frontiers in Chemistry

ORIGINAL RESEARCH
published: 19 March 2021
doi: 10.3389/fchem.2021.651248

Local Substrate Heterogeneity Influences Electrochemical Activity of TEM Grid-Supported Battery Particles

*Christina Cashen, R. Colby Evans, Zach N. Nilsson and Justin B. Sambur**

Department of Chemistry, Colorado State University, Fort Collins, CO, United States

Understanding how particle size and morphology influence ion insertion dynamics is critical for a wide range of electrochemical applications including energy storage and electrochromic smart windows. One strategy to reveal such structure–property relationships is to perform *ex situ* transmission electron microscopy (TEM) of nanoparticles that have been cycled on TEM grid electrodes. One drawback of this approach is that images of some particles are correlated with the electrochemical response of the entire TEM grid electrode. The lack of one-to-one electrochemical-to-structural information complicates interpretation of genuine structure/property relationships. Developing high-throughput *ex situ* single particle-level analytical techniques that effectively link electrochemical behavior with structural properties could accelerate the discovery of critical structure-property relationships. Here, using Li-ion insertion in WO_3 nanorods as a model system, we demonstrate a correlated optically-detected electrochemistry and TEM technique that measures electrochemical behavior of via many particles simultaneously without having to make electrical contacts to single particles on the TEM grid. This correlated optical-TEM approach can link particle structure with electrochemical behavior at the single particle-level. Our measurements revealed significant electrochemical activity heterogeneity among particles. Single particle activity correlated with distinct local mechanical or electrical properties of the amorphous carbon film of the TEM grid, leading to active and inactive particles. The results are significant for correlated electrochemical/TEM imaging studies that aim to reveal structure-property relationships using single particle-level imaging and ensemble-level electrochemistry.

Keywords: single particle electrochemistry, correlated imaging, ion insertion dynamics, electrochromism, optically detected electrochemistry

OPEN ACCESS

Edited by:
Mario A. Alpuche-Aviles, University of Nevada, Reno, United States

Reviewed by:
Jianping Huang, Lawrence Berkeley National Laboratory, United States
Zhiyuan Zeng, City University of Hong Kong, Hong Kong

****Correspondence:***
Justin B. Sambur
jsambur@colostate.edu

Specialty section:
This article was submitted to Electrochemistry, a section of the journal Frontiers in Chemistry

Received: *11 January 2021*
Accepted: *01 March 2021*
Published: *19 March 2021*

Citation:
Cashen C, Evans RC, Nilsson ZN and Sambur JB (2021) Local Substrate Heterogeneity Influences Electrochemical Activity of TEM Grid-Supported Battery Particles. Front. Chem. 9:651248. doi: 10.3389/fchem.2021.651248

INTRODUCTION

Nanoscale materials are attractive ion insertion hosts for applications such as electrochemical energy conversion and electrochromic smart windows (Bourderau et al., 1999; Li et al., 1999; Graetz et al., 2003; Arico et al., 2005; Manthiram et al., 2008). Their small dimensions minimize charge and ion transport distances, facilitating rapid and reversible charge injection and extraction. However, individual nanoparticles in a sample batch vary in size, shape, and surface structural sites.

Understanding how variations among particles contribute to ion insertion dynamics is critical to the design and optimization of electrodes.

Toward this goal, single particle-level electrochemical methods have been applied to battery materials (Heubner et al., 2020). Single particle-level electrochemical measurements reveal underlying ion and electron transport processes that are fundamentally related to solid state chemistry and the solid/electrolyte interface (Nelson et al., 2017; Wolf et al., 2017; Li et al., 2018; Yu et al., 2018). Scanning probe electrochemical methods have been used to uncover heterogeneous electrochemical activity of $LiFePO_4$ and $LiMn_2O_4$ battery particles (Kumatani et al., 2014; Tao et al., 2019). Similarly, Tao and co-workers pioneered a widefield plasmonic-based imaging method that has been used to distinguish Li-ion insertion/extraction behavior among $LiCoO_2$ nanoaprticles (Jiang et al., 2016). Several groups have attached battery particles to single nano- or micro-electrodes, extracting critical solid state diffusion and interfacial charge transfer rate constants (Jebaraj and Scherson, 2012; Tsai et al., 2018). All the above approaches possess advantages and disadvantages with respect to spatial/temporal resolution and throughput (Heubner et al., 2020). A major disadvantage of the *ex situ* approach is that it removes any possibility of correlating real-time electrochemical and structural dynamics. Another major challenge is that the aforementioned single particle-level methods typically correlate electrochemical and composition/structure information using *ex situ* scanning electron microscopy (SEM). Imaging may be performed before and after single particle-level electrochemical measurements, effectively linking single particle-level electrochemical and structural information. However, the limited spatial resolution of SEM imaging does not permit discovery of atomic scale structure–property relationships.

On the other hand, several atomic-level imaging methods have been used to study ion insertion kinetics of nanoparticle film or slurry electrodes (De Marco and Veder, 2010; Harks et al., 2015; Grey and Tarascon, 2017; Yuan et al., 2017; Tripathi et al., 2018; Boebinger et al., 2020; Li et al., 2020). Transmission electron microscopy (TEM; Huang et al., 2010; Liu and Huang, 2011; Liu et al., 2012; Zeng et al., 2014, 2020; Qi et al., 2016; Xie et al., 2017) and X-ray (Totir et al., 1997; Ota et al., 2003; Deb et al., 2004; Kim and Chung, 2004; Chao et al., 2010; Shearing et al., 2011; Nelson et al., 2012, 2017; Li et al., 2014, 2018; Shapiro et al., 2014; Wolf et al., 2017; Yau et al., 2017; Yu et al., 2018) imaging methods have measured the real-time lithiation kinetics of nanoparticle electrodes and have successfully incorporated material properties such as film porosity, particle shape, orientation, and composition to predict the system's electrochemical response (Garcia et al., 2005; Gupta et al., 2011; Stephenson et al., 2011; Ebner et al., 2014; Landesfeind et al., 2018). *In situ* single particle-level TEM measurements have revealed dynamic structural information of battery materials (Huang et al., 2010). However, the *in situ* TEM technique requires vacuum or quasi vacuum operation conditions and the *in situ* sample holder and sample preparations steps are complicated, leading to low-throughput (Wu and Liu, 2018).

Expanding the scope of high-throughput *ex situ* single particle-level analytical techniques that effectively link electrochemical behavior with structural properties could help uncover important design principles for battery and related functional materials. One strategy that has been applied to nanofibers (Zhang et al., 2018), electrocatalysts (Yu et al., 2012; Arán-Ais et al., 2015), and battery materials (Wang et al., 1999; Lee et al., 2019) is to measure the electrochemical response of the entire electrode and link that response to structural changes of single particles revealed by TEM imaging. Tracking the same particles over time can reveal how electrochemical cycling induces structural transformations. The electrochemical behavior of single battery particles may be inferred from the ensemble-level electrochemical response (Zhang et al., 2020). Inferring single particle-level electrochemical responses from the ensemble-average system response assumes some level of homogeneous activity across the population. One issue is that the TEM grid substrate material has different electrical and mechanical properties than more common metal substrates (e.g., Cu and Ti foil). Hence, understanding the role of the TEM grid support on the electrochemical behavior of particles is important for interpreting *ex situ* TEM results with ensemble-level electrochemical data.

Here, we introduce an optically-detected electrochemical approach that uses a conventional bright field optical microscope to acquire single particle electrochemical data and *ex situ* TEM characterization of single nanoparticles in a one-to-one fashion. The measurements relate the optical density (OD) change of single nanoparticles to redox changes in the particle. We demonstrate the method using Li-ion insertion in tungsten oxide nanorods (NRs) as a model system. The optical signal is insensitive to electrical double layer charging but sensitive to redox changes of elements in the particle (e.g., W^{6+}/W^{5+} in WO_3). Widefield optical imaging has been used to characterize Li-ion insertion in electrochromic WO_3 and MoO_3 thin films (McEvoy and Stevenson, 2003, 2005a,b; Kondrachova et al., 2009) and battery materials at the ensemble- and single microparticle-levels (Harris et al., 2010; Love et al., 2015; Duay et al., 2016; Wood et al., 2016; Sanchez et al., 2020), but the aforementioned studies have not linked electrochemical and composition/structural analysis at the single particle-levels. This widefield approach enables one-to-one electrochemical-to-structural characterization of tens to hundreds of particles in a single experiment, limited by the coverage of single particles on the TEM substrate.

EXPERIMENTAL METHODS

Synthesis and Characterization

Hexagonal WO_3 (h-WO_3) NRs were synthesized via a hydrothermal reaction that was developed by Wang et al. (2008). We added 0.5798 g of NaCl (Fisher Scientific) and 0.8250 g of $Na_2WO_4 \bullet 2H_2O$ (Mallinckrodt Chemical Works) to 19 ml of 18.2 MΩ-cm H_2O. Then, under continuous stirring, 3 M HCl was slowly added to adjust the solution pH to 2.06. This procedure typically required 850 μL of 3 M HCl. The pH was monitored by a HQ11d pH probe (Hach). This solution was

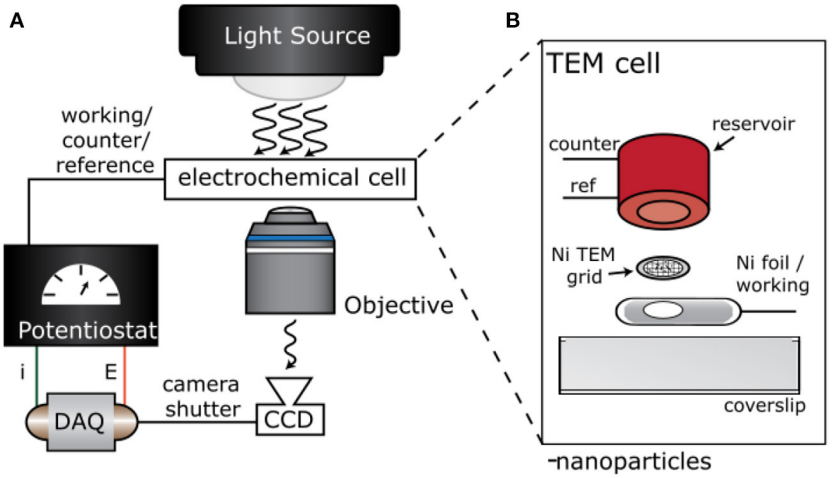

FIGURE 1 | Experimental setup and electrochemical cell design. Cartoon illustration of the **(A)** experimental setup for single particle electro-optical imaging experiments and **(B)** electrochemical cell with a TEM grid working electrode.

then placed into a 23 ml Parr acid digest reactor and heated in a convection oven at 180°C for 24 h. After 24 h, the vessel was removed from the oven, placed on the bench top, and allowed to cool to room temperature. The supernatant was pipetted out of the vessel and the white powder product at the bottom of the vessel was transferred to a centrifuge tube, washed with 18.2 MΩ-cm H_2O, and stored in ethanol. The product was analyzed via powder X-ray diffraction (PXRD) using a Bruker D8 Discover Series II X-ray Diffractometer (PXRD), with Cu Kα (λ = 0.15406 nm) radiation at 50 kV and 50 mA in a 2θ range from 10° to 80° (**Supplementary Figure 1**). The PXRD experiments were carried out at room temperature on a zero-diffraction silicon wafer (MTI Chemical Corp).

Electrochemical Cell Assembly

Figure 1A shows a cartoon illustration of the experimental setup and electrochemical cell design. We designed an optically transparent electrochemical cell with a TEM grid working electrode. To do so, we drop-casted a 1 mg/ml ethanol solution of WO_3 nanoparticles on a Ni TEM Grid (Ted Pella PELCO® 200 Mesh Ni Grid, pure carbon). The TEM grid was sandwiched between a 3D printed polyethylene terephthalate glycol (PETG) reservoir and a small piece of Ni foil (Sigma-Aldrich, >99.9% Ni), as shown in **Figure 1B**. The Pt counter (CE) and Ag/AgCl reference (RE) electrodes were secured in a 3D-printed PETG reservoir via pre-drilled holes and epoxy (**Figure 1B**). The grid was placed above a 3 mm hole in the Ni foil that was cut with a tap and dye set. Once the TEM grid was sandwiched between the coverslip, Ni foil, and reservoir, the entire assembly was mechanically secured using insulating epoxy (Loctite E-120HP Hysol). A digital multimeter confirmed that the TEM grid and Ni foil remained in good electrical contact throughout the assembly process.

Electro-Optical Imaging Experiments

The experimental setup and detailed image analysis procedures are provided in our previous publications (Evans et al., 2019a,b). Briefly, the electrode assembly was mounted on the motorized XY stage of an Olympus IX-73 optical microscope. Bright field transmission images were acquired at a 100 ms frame rate and under 940 nm light emitting diode (LED, Thor Labs) excitation. The light was collected by a 100× objective (UPLANSAPO100x/W) and imaged on an Andor (iXON 897) EM-CCD detector. A 2× magnification lens was inserted into the beam path to achieve 200× magnification. Chronoamperometry measurements were conducted in 1 M $LiClO_4$ (Aldrich) in propylene carbonate (Aldrich) using a potentiostat (Metrohm Autolab PGSTAT128N). Cathodic and anodic potential steps were applied for 30 s between −1.0 and +0.5 V vs. Ag/AgCl, respectively. The applied potential, electrochemical current, and EM-CCD camera shutter signals were acquired simultaneously via a data acquisition card (DAQ) to precisely synchronize the signals (Evans et al., 2019b). This data synchronization enables each image in the stack or "movie" to be indexed to the time and potential as measured by the potentiostat.

Electron Microscopy

Ex situ electron microscopy experiments were performed after the electro-optical imaging experiments. The TEM grid was mechanically removed from the cell using a razor blade. The grid was gently washed with dimethyl carbonate (Sigma) and dried in a N_2 stream. Transmission electron microscopy images were collected on a JOEL JEM-2100F electron microscope at a working voltage of 200 keV.

Image Analysis Procedures

We developed an image analysis procedure to overlay the optical and electron microscopy images. The first step of the procedure is to identify control point pairs in both images. For example,

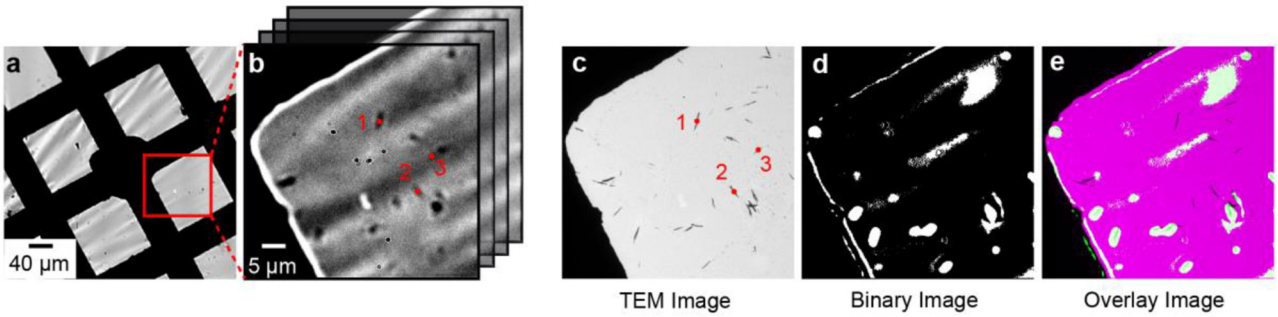

FIGURE 2 | Correlated electro-optical and TEM imaging. **(a,b)** Bright field optical microscope image of a WO_3-coated TEM grid working electrode at 10× and 60× magnification, respectively. **(b)** Imaging stack showing the continuous imaging sequence in the electro-optical imaging experiment. The centroid positions of single particles are indicated by the red dots labeled 1, 2, and 3. **(c)** TEM image of the sample region in **(b)**. The red dots represent the centroids of individual particles. **(d)** Binary optical image of WO_3 nanorods. White pixels correspond to OD-values that were >10-times the standard deviation of the background. **(e)** Overlay of the binary image on the TEM image.

the points labeled 1, 2, and 3 in **Figure 2b** represent the centroid positions of three individual nanorods that were determined using the centroid function in MATLAB's image processing toolbox. **Figure 2c** shows a TEM image of the same sample region in **Figure 2b** and the points labeled 1, 2, and 3 represent the centroid positions of the same nanorods. We use the imtransform function in MATLAB to overlay the optical image onto the TEM image using the spatial transformation defined by the control point pairs. Active particles were classified as active if the OD-value exceeded the mean + 3 standard deviations of the background OD.

We developed an intensity-based algorithm to assign particles and particle clusters to specific background region types, as discussed later in the manuscript. We identified four background region types and analyzed intensity vs. time trajectories from each region. We used the mean and standard deviation values of Type 4 areas as criteria for assignment. Single particles and clusters were assigned to Type 1 regions if, following a polarization pulse, the OD intensity surrounding a particle was less than the mean – 3 standard deviations of Type 4 regions. If the particles could not be assigned to Type 1 regions, then they were assigned to Type 3 regions if the standard deviation of the background exceeded 3× the standard deviation of Type 4 areas. If the particles could not be assigned to Type 1 or 3 regions, then they were assigned to Type 4 regions. We omitted the three particles that could be assigned to a Type 2 region because the results were not statistically meaningful.

RESULTS AND DISCUSSION

We used bright field optical microscopy to measure the rate of Li-ion insertion in single WO_3 nanorods. In a typical experiment, WO_3 nanorods were drop-casted on the TEM grid and assembled into a 3-electrode electrochemical cell as shown in **Figure 1**. The average length and width of the nanorods were 1.02 ± 0.54 and 0.10 ± 0.04 μm, respectively, as determined by electron microscopy (Evans et al., 2019a). **Figures 2a,b** shows 10× and 60× magnification optical transmission images of the WO_3 nanorod-coated TEM grid working electrode before lithiation. The nanorods appear as dark objects against a bright background because the nanorods absorb and scatter incident light. **Figure 2c** shows a TEM image of the same sample region as in **Figures 2a,b**. The amorphous carbon film of the TEM membrane is expectedly transparent in the electron microscope but the material is not fully transparent in the optical microscope, which has important consequences for the electro-optical imaging experiment, as discussed in detail below.

We studied the dynamic optical properties of these electrochromic h-WO_3 NRs during chronoamperometry experiments. To induce Li-ion insertion in the h-WO_3 NRs according to Equation (1), a cathodic potential step of −1.0 V vs. Ag/AgCl was applied to the TEM grid electrode while a series of bright field transmission images were acquired at a 100 ms frame rate (**Figure 2b**). The lithiation reaction increases the OD of the sample due to the formation of [Li^+-W^{5+}] color centers (Bohnke et al., 1992; Vuillemin and Bohnke, 1994), causing the compound to turn dark blue. Applying an anodic potential of +0.5 V induces the delithiation reaction, causing the blue compound to return to a more transparent state (W^{6+}).

$$WO_3 + xLi^+ + xe^- \leftrightarrow Li_xWO_3 \quad (1)$$

The electro-optical measurements relate OD as a function of polarization time, $\Delta OD(t)$, to the concentration of [Li-W^{5+}] color centers as a function of time, $c(t)$, using the Beer-Lambert law according to Equation (2) (valid for $x < 0.5$) (Denesuk and Uhlmann, 1996; Scarminio et al., 1999; Wen et al., 2015), where ε_λ is the monochromatic molar absorption coefficient (10^6 cm^2/mol at 930 nm; Vuillemin and Bohnke, 1994) and d is the particle thickness. We measure $\Delta OD(t)$ by calculating the intensities of the incident and transmitted light through the amorphous carbon film of the TEM grid working electrode and WO_3 particles, $I_0(t)$ and $I(t)$, respectively, as a function of time.

We determine d from electron microscopy images and assume that the nanorod cross section can be approximated as a square rectangle, as supported by atomic force microscopy data (Evans et al., 2019a).

$$\Delta OD\,(t) = \varepsilon_\lambda c\,(t)\,d = -\log_{10}\frac{I\,(t)}{I_0\,(t)} + \log_{10}\frac{I(0)}{I_0(0)} \qquad (2)$$

To identify OD changes of objects during the cathodic polarization pulse, we thresholded the final image by subtracting the initial image (delithiated particles) from the final image at the end of the cathodic potential step (lithiated particles) to form a binary image. **Figure 2d** shows the result of the thresholding procedure, where white pixels indicate an OD increase resulting from the potential step. Finally, we overlay the binary image in **Figure 2d** on the TEM image using the image analysis procedure described in the Experimental Methods section. The white pixels located on dark objects in **Figure 2e** represent single WO_3 NRs or WO_3 NR clusters whose OD increases during the cathodic potential pulse and, therefore, those particles that are active for the lithiation reaction.

Having developed an image processing algorithm to assess electrochemical activity of WO_3 NRs in an unbiased way, we studied the electrochemical activity of 6 single WO_3 NRs and 83 WO_3 NR clusters consisting of 2–15 NRs. We identified that 33% of individual NRs and 41% of NR clusters were electrochemically active, as evidenced by OD-values that exceeded the background threshold defined in the Experimental Methods section. **Figures 3a–c** and **Figures 3d–f** show representative ΔOD(t) trajectories from active and inactive WO_3 particles, respectively. Upon applying the cathodic potential step of −1.0 V vs. Ag/AgCl, one WO_3 particle cluster exhibits an OD increase (**Figures 3a–c**) whereas another WO_3 particle (**Figures 3d–f**) exhibits no clear OD change. In our previous study of the same WO_3 NR sample on indium doped tin oxide (ITO) electrodes, we observed only 9 out of 102, or 9%, of these h-WO_3 NRs were inactive (Evans et al., 2019a). In addition, we observed that 349 clusters contained 1–25 NRs were electrochemically active. The high percentage of active clusters on ITO substrates is likely due to the fact that the probability of forming a cluster from two inactive single particles is only 0.8%. The particle–particle interfaces and contact area between particles in clusters influence OD dynamics, not overall activity (Evans et al., 2019a). Since the electrolyte and WO_3 materials in those measurements were identical to those used in this work, we attribute the large inactive particle population in this study to a poor electrical contact between the WO_3 particles and the amorphous carbon film of the TEM grid. This result remains hidden in the electrochemical current-potential data because the signal stems from the entire TEM grid electrode.

To understand the origin of the large inactive population, we first examined the behavior of the amorphous carbon film substrate. We observed that bare regions of the amorphous carbon film exhibit an OD increase after the potential step even though no WO_3 particles appear in that region (**Figure 2e**). To understand the role of the applied potential on the OD

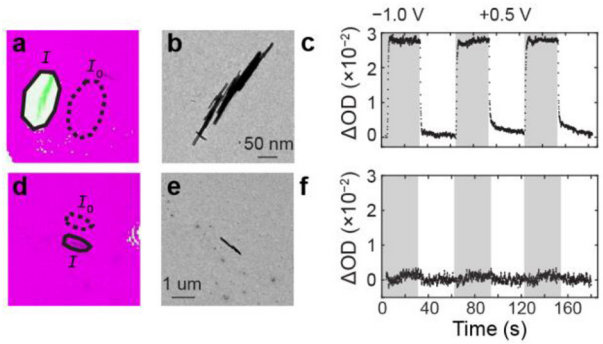

FIGURE 3 | ΔOD(t) kinetics of active and inactive WO_3 particles. **(a)** Optical and TEM overlay image. The solid and dashed ovals represent the I and I_0 pixel regions that were used to calculate the OD trajectories. **(b)** TEM image of an active WO_3 particle cluster. **(c)** ΔOD(t) trajectory of the particle cluster in **(a,b)**. The gray and white vertical bars represent the time windows of the cathodic and anodic potential steps. **(d–f)** same as **(a–c)** but for an inactive h-WO_3 NR.

increase, we analyzed the OD dynamics of the amorphous carbon substrate. **Figures 4A–C** shows a sequence of bright field transmission images during the electro-optical imaging experiment. The image brightness and contrast were adjusted to highlight the small pixel intensity changes of the amorphous carbon film. **Figure 4D** shows a normalized intensity vs. time trajectory of the blank amorphous carbon film region (yellow oval in **Figures 4A–C**). The OD intensity changes immediately upon applying the cathodic potential pulse and decays exponentially with time. We attribute this exponential decay behavior to a mechanical response of the amorphous carbon film during the electrical double layer charging process of the membrane, which also occurs exponentially with time (Bard and Faulkner, 2001). The slow OD decay compared to electrical double layer charging is likely due to the slow mechanical motion of the film in the electrolyte. In this scenario, the OD increases because the membrane material folds into the region of space that is sampled in a single 222 × 222 nm^2 pixel.

We identified four types of mechanical behaviors after surveying 89 regions of the bare amorphous carbon film. **Figures 5A,B** shows four representative OD trajectories from different regions of the amorphous carbon-film. All regions show an overall OD decrease during the initial cathodic polarization pulse. This behavior suggests that the film stretches or bends, either during electrical double layer formation or upon lithiation of the amorphous carbon (Li and Wang, 2020), and then returns contracts to an initial state after cathodic polarization. After the initial pulse, Type 1 regions exhibit a sharp OD decrease upon applying a potential step, regardless of the polarization potential, followed by an OD increase during the cathodic polarization step. On the other hand, Type 2 regions exhibit a slow OD increase upon applying anodic potentials and a sharp OD decrease at cathodic polarization potentials. In this case, the electrode polarization influences the apparent thinning of the amorphous carbon material in the region of interest. That OD increases in one region and decreases in another suggests

that the film could be stretching in some regions and bunching up in others. Type 3 regions exhibit slow, anomalous changes that can be linked to the polarization pulse whereas Type 4 regions show no optical changes, which could be due to either insulating areas of the amorphous carbon film or mechanically robust regions.

We hypothesized that the electrochemical activity could be linked to the local behaviors of the underlying amorphous carbon film. To test this hypothesis, we examined the OD behavior of the amorphous carbon film surrounding each particle. Then, we assigned each h-WO_3 NR to a population based on that local film behavior. **Figure 6** shows the distribution of OD-values for 6 single WO_3 NRs and 83 WO_3 NR clusters for Type 1, 3, and 4 regions. We omit the three particles that were assigned to a Type 2 region because the results are not statistically meaningful, likely due to the fact that this type of mechanical behavior is not present across a large fraction of the TEM membrane material. The largest, but least active, particle population was WO_3 particles in Type 4 areas. Here, we define active particles as those whose OD exceeds the average OD-value from Type 4 areas plus three standard deviations. The large inactive population could be due to the insulating nature of the TEM membrane material because we observed that Type 4 material did not respond to potential steps (**Figure 5B**). Less particles were observed in Type 1 and 3

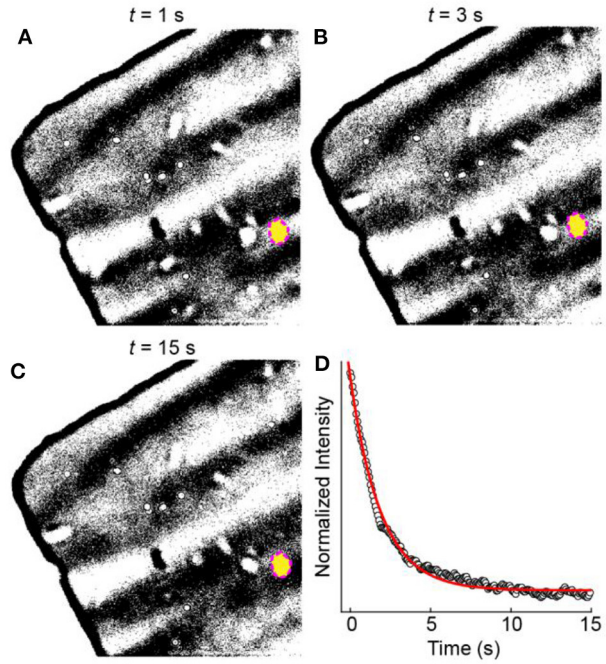

FIGURE 4 | OD changes of the TEM membrane. **(A–C)** Optical microscope images as a function of time during a cathodic potential step experiment. **(D)** Normalized intensity vs. time trajectory (black circles) from the region of interest indicated by the yellow circle in **(A–C)**. The red line represents a fit to an exponential decay function.

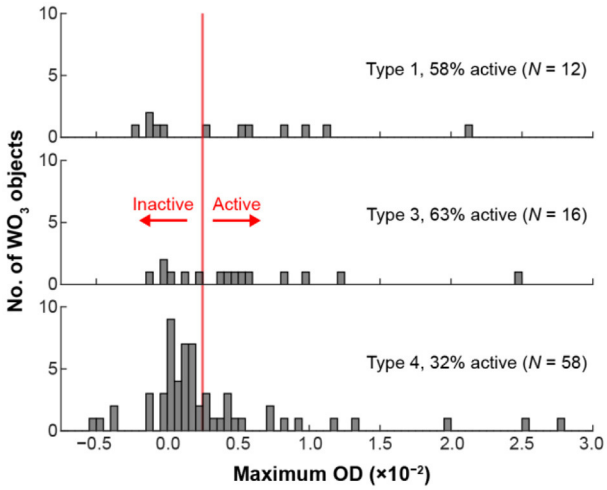

FIGURE 6 | Distribution of maximum OD-values from 6 single WO_3 NRs and 83 WO_3 NR clusters consisting of 2–15 NRs located in different regions of the TEM grid. The TEM grid types were defined in **Figure 5** (see main text for discussion).

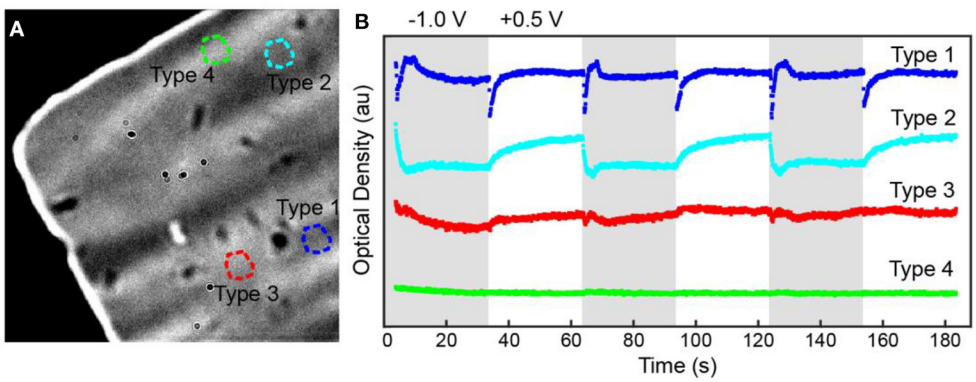

FIGURE 5 | (A) Transmission image and **(B)** OD trajectories measured from four different substrate regions, labeled Type 1, 2, 3, and 4 in **(A)**.

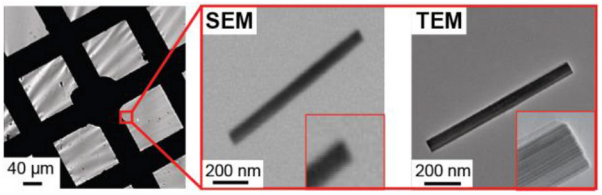

FIGURE 7 | Comparison of SEM and TEM imaging results of the same single h-WO_3 NR on the TEM grid working electrode.

areas, but those particles were, on average, more active. Type 1 and 3 areas are likely conductive regions because the material responds to the potential step (**Figure 5B**), which could explain the higher fraction of active particles in Type 1 and 3 regions.

Regardless of the underlying origin of the activity distributions in **Figure 6**, we conclude that the local mechanical properties of the TEM membrane influence the electrochemical activity of the h-WO_3 NRs. It may be possible to test this hypothesis by making local force measurements using an atomic force microscope. Our results have broader implications for correlated electrochemical and *ex situ* TEM measurements that link ensemble-level electrochemical data with *ex situ* TEM imaging. The electrochemical current of TEM membrane-supported particles may not reflect the current on other current collectors and the current may vary from particle-to-particle due to support interactions.

An important aspect of this work that goes beyond our previous study is that correlated TEM imaging reveals atomic level structural detail that cannot be achieved with correlated SEM imaging, as is typically done in the field of single particle electrochemistry. **Figure 7** compares SEM and TEM imaging of a single h-WO_3 NR on the TEM grid working electrode. High resolution SEM imaging does not reveal atomic level structural features that appear in the TEM image. This capability will enable future studies that elucidate the role of intraparticle structural properties on single particle electrochemical behavior.

CONCLUSIONS

We developed a correlated optically-detected electrochemistry/*ex situ* TEM imaging approach to study the electrochemical activity of single particles on a TEM grid electrode. The methodology presented herein can be applied generally to numerous electrochemical systems that exhibit optical property changes during electrochemical cycling (e.g., electrochromic smart windows, batteries, solid oxide fuel cells, and sensors). In the context of energy storage, the optical microscopy can be applied to study electrochromic materials such as $LiCoO_2$ (Švegl et al., 2000), $LiFePO_4$ (Zaghib et al., 2007), and $Li_4Ti_5O_{12}$ (Yu et al., 2010; Li et al., 2019). The technique can be performed in reflectance mode on opaque current collectors such as Al, Ni, or Cu foil and is not limited to transparent current collectors. This analytical technique leverages a conventional bright field optical microscope to obtain single particle electrochemistry data and is compatible with existing TEM (Huang et al., 2010; Liu and Huang, 2011; Liu et al., 2012; Qi et al., 2016; Xie et al., 2017; Tu et al., 2018; Zhang et al., 2020) and X-ray (Totir et al., 1997; Ota et al., 2003; Deb et al., 2004; Kim and Chung, 2004; Chao et al., 2010; Shearing et al., 2011; Nelson et al., 2012, 2017; Shapiro et al., 2014; Wolf et al., 2017; Yau et al., 2017; Li et al., 2018; Yu et al., 2018) micro-spectroscopy methods.

DATA AVAILABILITY STATEMENT

The raw data supporting the conclusions of this article will be made available by the authors, without undue reservation.

AUTHOR CONTRIBUTIONS

CC and RE performed experiments, analyzed data, and wrote the manuscript. ZN performed TEM measurements. JS analyzed data and wrote the manuscript. All authors contributed to the article and approved the submitted version.

FUNDING

This work was support by the National Science Foundation (DMR-2046948).

SUPPLEMENTARY MATERIAL

The Supplementary Material for this article can be found online at: https://www.frontiersin.org/articles/10.3389/fchem.2021.651248/full#supplementary-material

REFERENCES

Arán-Ais, R. M., Yu, Y., Hovden, R., Solla-Gullón, J., Herrero, E., Feliu, J. M., et al. (2015). Identical location transmission electron microscopy imaging of site-selective Pt nanocatalysts: electrochemical activation and surface disordering. *J. Am. Chem. Soc.* 137, 14992–14998. doi: 10.1021/jacs.5b09553

Arico, A., Bruce, P. G., Scrosati, B., Tarascon, J.-M., and Schalkwijk, W. (2005). Nanostructured materials for advanced energy conversion and storage devices. *Nat. Mater.* 4, 366–377. doi: 10.1038/nmat1368

Bard, A. J., and Faulkner, L. R. (2001). *Electrochemical Methods : Fundamentals and Applications, 2nd Edn.* New York, NY : Wiley, New York.

Boebinger, M. G., Lewis, J. A., Sandoval, S. E., and McDowell, M. T. (2020). Understanding transformations in battery materials using *in situ* and operando experiments: progress and outlook. *ACS Energy Lett.* 5, 335–345. doi: 10.1021/acsenergylett.9b02514

Bohnke, O., Rezrazi, M., Vuillemin, B., and Bohnké, C. (1992). "*In situ*" optical and electrochemical characterization of electrochromic phenomena into tungsten trioxide thin films. *Sol. Energy Mater.* 25, 361–374. doi: 10.1016/0927-0248(92)90080-9

Bourderau, S., Brousse, T., and Schleich, D. M. (1999). Amorphous silicon as a possible anode material for Li-ion batteries. *J. Power Sources* 81–82, 233–236. doi: 10.1016/S0378-7753(99)00194-9

Chao, S.-C., Yen, Y.-C., Song, Y.-F., Chen, Y.-M., Wu, H.-C., and Wu, N.-L. (2010). A study on the interior microstructures of working Sn particle electrode of Li-ion batteries by *in situ* X-ray transmission microscopy. *Electrochem. Commun.* 12, 234–237. doi: 10.1016/j.elecom.2009.12.002

De Marco, R., and Veder, J.-P. (2010). *In situ* structural characterization of electrochemical systems using synchrotron-radiation techniques. *Trends Anal. Chem.* 29, 528–537. doi: 10.1016/j.trac.2010.01.011

Deb, A., Bergmann, U., Cairns, E. J., and Cramer, S. P. (2004). X-Ray absorption spectroscopy study of the $LixFePO_4$ cathode during cycling using a novel electrochemical *in situ* reaction cell. *J. Synchrotron Radiat.* 11, 497–504. doi: 10.1107/S0909049504024641

Denesuk, M., and Uhlmann, D. R. (1996). Site-saturation model for the optical efficiency of tungsten oxide-based devices. *J. Electrochem. Soc.* 143, L186–L188. doi: 10.1149/1.1837080

Duay, J., Schroder, K. W., Murugesan, S., and Stevenson, K. J. (2016). Monitoring volumetric changes in silicon thin-film anodes through *in situ* optical diffraction microscopy. *ACS Appl. Mater. Interfaces* 8, 17642–17650. doi: 10.1021/acsami.6b03822

Ebner, M., Chung, D.-W., and Edwin, G. R., amd Vanessa, W. (2014). Tortuosity anisotropy in lithium-ion battery electrodes. *Adv. Energy Mater.* 4:1301278. doi: 10.1002/aenm.201301278

Evans, R. C., Ellingworth, A., Cashen, C. J., Weinberger, C. R., and Sambur, J. B. (2019a). Influence of single-nanoparticle electrochromic dynamics on the durability and speed of smart windows. *Proc. Natl. Acad. Sci. U.S.A.* 116, 12666–12671. doi: 10.1073/pnas.1822007116

Evans, R. C., Nilsson, Z. N., and Sambur, J. B. (2019b). High-throughput single-nanoparticle-level imaging of electrochemical ion insertion reactions. *Anal. Chem.* 91, 14983–14991. doi: 10.1021/acs.analchem.9b03487

Garcia, R. E., Chiang, Y.-M., Craig Carter, W., Limthongkul, P., and Bishop, C. M. (2005). Microstructural modeling and design of rechargeable lithium-ion batteries. *J. Electrochem. Soc.* 152, A255–A259. doi: 10.1149/1.1836132

Graetz, J., Ahn, C. C., Yazami, R., and Fultz, B. (2003). Highly reversible lithium storage in nanostructured silicon. *Electrochem. Solid-State Lett.* 6, A194–A197. doi: 10.1149/1.1596917

Grey, C. P., and Tarascon, J. M. (2017). Sustainability and *in situ* monitoring in battery development. *Nat. Mater.* 16, 45–56. doi: 10.1038/nmat4777

Gupta, A., Seo, J. H., Zhang, X. C., Du, W. B., Sastry, A. M., and Shyy, W. (2011). Effective transport properties of $LiMn_2O_4$ electrode via particle-scale modeling. *J. Electrochem. Soc.* 158, A487–A497. doi: 10.1149/1.3560441

Harks, P. P. R. M. L., Mulder, F. M., and Notten, P. H. L. (2015). *In situ* methods for Li-ion battery research: a review of recent developments. *J. Power Sources* 288, 92–105. doi: 10.1016/j.jpowsour.2015.04.084

Harris, S. J., Timmons, A., Baker, D. R., and Monroe, C. (2010). Direct *in situ* measurements of Li transport in Li-ion battery negative electrodes. *Chem. Phys. Lett.* 485, 265–274. doi: 10.1016/j.cplett.2009.12.033

Heubner, C., Langklotz, U., Lämmel, C., Schneider, M., and Michaelis, A. (2020). Electrochemical single-particle measurements of electrode materials for Li-ion batteries: possibilities, insights and implications for future development. *Electrochim. Acta* 330:135160. doi: 10.1016/j.electacta.2019.135160

Huang, J., Zhong, L., Wang, C., Sullivan, J., and Xu, W. (2010). *In situ* observation of the electrochemical lithiation of a single SnO_2 nanowire electrode. *Science* 330, 1515–1520. doi: 10.1126/science.1195628

Jebaraj, A. J. J., and Scherson, D. A. (2012). Microparticle electrodes and single particle microbatteries: electrochemical and *in situ* microraman spectroscopic studies. *Acc. Chem. Res.* 46, 1192–1205. doi: 10.1021/ar300210q

Jiang, D., Jiang, Y., Li, Z., Liu, T., Wo, X., Fang, Y., et al. (2016). Optical imaging of phase transition and Li-ion diffusion kinetics of single $LiCoO_2$ nanoparticles during electrochemical cycling. *J. Am. Chem. Soc.* 139, 186–192. doi: 10.1021/jacs.6b08923

Kim, J.-M., and Chung, H.-T. (2004). The first cycle characteristics of $Li[Ni_{1/3}Co_{1/3}Mn_{1/3}]O_2$ charged up to 4.7 V. *Electrochim. Acta* 49, 937–944. doi: 10.1016/j.electacta.2003.10.005

Kondrachova, L. V., May, R. A., Cone, C. W., Vanden Bout, D. A., and Stevenson, K. J. (2009). Evaluation of lithium ion insertion reactivity via electrochromic diffraction-based imaging. *Langmuir* 25, 2508–2518. doi: 10.1021/la803245a

Kumatani, A., Munakata, H., Inomata, H., Ito, K., Ino, K., Shiku, H., et al. (2014). Nanoscale Visualization of redox activity at lithium-ion battery cathodes. *Nat. Commun.* 5:5450. doi: 10.1038/ncomms6450

Landesfeind, J., Ebner, M., Eldiven, A., Wood, V., and Gasteiger, H. A. (2018). Tortuosity of battery electrodes: validation of impedance-derived values and critical comparison with 3D tomography. *J. Electrochem. Soc.* 165, A469–A476. doi: 10.1149/2.0231803jes

Lee, S.-Y., Park, G.-S., Jung, C., Ko, D.-S., Park, S.-Y., Kim, H. G., et al. (2019). Revisiting primary particles in layered lithium transition-metal oxides and their impact on structural degradation. *Adv. Sci.* 6:1800843. doi: 10.1002/advs.201800843

Li, D., and Wang, Y. (2020). *In-situ* measurements of mechanical property and stress evolution of commercial graphite electrode. *Mater. Des.* 194:108887. doi: 10.1016/j.matdes.2020.108887

Li, H., Huang, X., Chen, L., Wu, Z., and Liang, Y. (1999). A high capacity nano Si composite anode material for lithium rechargeable batteries. *Electrochem. Solid State Lett.* 2, 547–549. doi: 10.1149/1.1390899

Li, M., Gould, T., Su, Z., Li, S., Pan, F., and Zhang, S. (2019). Electrochromic properties of $Li_4Ti_5O_{12}$: from visible to infrared spectrum. *Appl. Phys. Lett.* 115:073902. doi: 10.1063/1.5099330

Li, T., Kang, H., Zhou, X., Lim, C., Yan, B., De Andrade, V., et al. (2018). Three-dimensional reconstruction and analysis of all-solid Li-ion battery electrode using synchrotron transmission X-ray microscopy tomography. *ACS Appl. Mater. Interfaces* 10, 16927–16931. doi: 10.1021/acsami.7b18962

Li, W., Lutz, D. M., Wang, L., Takeuchi, K. J., Marschilok, A. C., Takeuchi, E. S., (2020). Peering into batteries: electrochemical insight through *in situ* and operando methods over multiple length scales. *Joule* 5, 77–88. doi: 10.1016/j.joule.2020.11.003

Li, Y., El Gabaly, F., Ferguson, T. R., Smith, R. B., Bartelt, N. C., Sugar, J. D., et al. (2014). Current-induced transition from particle-by-particle to concurrent intercalation in phase-separating battery electrodes. *Nat. Mater.* 13, 1149–1156. doi: 10.1038/nmat4084

Liu, X. H., and Huang, J. Y. (2011). *In situ* TEM electrochemistry of anode materials in lithium ion batteries. *Energy Env. Sci* 4, 3844–3817. doi: 10.1039/c1ee01918j

Liu, X. H., Wang, J. W., Huang, S., Fan, F., Huang, X., Liu, Y., et al. (2012). *In situ* atomic-scale imaging of electrochemical lithiation in silicon. *Nat. Nanotechnol.* 7, 749–756. doi: 10.1038/nnano.2012.170

Love, C. T., Baturina, O. A., and Swider-Lyons, K. E. (2015). Observation of lithium dendrites at ambient temperature and below. *ECS Electrochem. Lett.* 4, A24–A27. doi: 10.1149/2.0041502eel

Manthiram, A., Vadivel Murugan, A., Sarkar, A., and Muraliganth, T. (2008). Nanostructured electrode materials for electrochemical energy storage and conversion. *Energy Environ. Sci.* 1, 621–638. doi: 10.1039/B811802G

McEvoy, T. M., and Stevenson, K. J. (2003). Spatially resolved measurement of inhomogeneous electrocoloration/insertion in polycrystalline molybdenum oxide thin films via chronoabsorptometric imaging. *J. Am. Chem. Soc.* 125, 8438–8439. doi: 10.1021/ja035370c

McEvoy, T. M., and Stevenson, K. J. (2005a). Spatially resolved imaging of inhomogeneous charge transfer behavior in polymorphous molybdenum oxide. I. Correlation of localized structural, electronic, and chemical properties using conductive probe atomic force microscopy and raman microprobe spectroscopy. *Langmuir* 21, 3521–3528. doi: 10.1021/la047276v

McEvoy, T. M., and Stevenson, K. J. (2005b). Spatially resolved imaging of inhomogeneous charge transfer behavior in polymorphous molybdenum oxide. II. Correlation of localized coloration/insertion properties using spectroelectrochemical microscopy. *Langmuir* 21, 3529–3538. doi: 10.1021/la047273i

Nelson, G. J., Ausderau, L. J., Shin, S., Buckley, J. R., Mistry, A., Mukherjee, P. P., et al. (2017). Transport-geometry interactions in Li-ion cathode materials imaged using x-ray nanotomography. *J. Electrochem. Soc.* 164, A1412–A1424. doi: 10.1149/2.0261707jes

Nelson, J., Misra, S., Yang, Y., Jackson, A., Liu, Y., Wang, H., et al. (2012). In operando X-ray diffraction and transmission X-ray microscopy of lithium sulfur batteries. J. Am. Chem. Soc. 134, 6337–6343. doi: 10.1021/ja2121926

Ota, H., Akai, T., Namita, H., Yamaguchi, S., and Nomura, M. (2003). XAFS and TOF–SIMS analysis of SEI layers on electrodes. *J. Power Sources* 119–121, 567–571. doi: 10.1016/S0378-7753(03)00291-X

Qi, K., Li, X., Sun, M., Huang, Q., Wei, J., Xu, Z., et al. (2016). *In-situ* transmission electron microscopy imaging of formation and evolution of Li XWO_3

during lithiation of WO_3 nanowires. *Appl. Phys. Lett.* 108, 233103–233105. doi: 10.1063/1.4950968

Sanchez, A. J., Kazyak, E., Chen, Y., Chen, K.-H., Pattison, E. R., and Dasgupta, N. P. (2020). Plan-view operando video microscopy of Li metal anodes: identifying the coupled relationships among nucleation, morphology, and reversibility. *ACS Energy Lett.* 5, 994–1004. doi: 10.1021/acsenergylett.0c00215

Scarminio, J., Urbano, A., and Gardes, B. (1999). The Beer-Lambert law for electrochromic tungsten oxide thin films. *Mater. Chem. Phys.* 61, 143–146. doi: 10.1016/S0254-0584(99)00132-7

Shapiro, D. A., Yu, Y.-S., Tyliszczak, T., Cabana, J., Celestre, R., Chao, W., et al. (2014). Chemical composition mapping with nanometre resolution by soft X-ray microscopy. *Nat. Photonics* 8, 765–769. doi: 10.1038/nphoton.2014.207

Shearing, P., Wu, Y., Harris, S. J., and Brandon, N. (2011). *In situ* X-ray spectroscopy and imaging of battery materials. *Electrochem. Soc. Interface* 20, 43–47. doi: 10.1149/2.F03113if

Stephenson, D. E., Walker, B. C., Skelton, C. B., Gorzkowski, E. P., Rowenhorst, D. J., and Wheeler, D. R. (2011). Modeling 3D microstructure and ion transport in porous Li-ion battery electrodes. *J. Electrochem. Soc.* 158, A781–A789. doi: 10.1149/1.3579996

Švegl, F., Orel, B., and Kaučič, V. (2000). Electrochromic properties of lithiated co-oxide ($LixCoO_2$) and Ni-oxide ($LixNiO_2$) thin films prepared by the sol–gel route. *Sol. Energy* 68, 523–540. doi: 10.1016/S0038-092X(00)00028-1

Tao, B., Yule, L. C., Daviddi, E., Bentley, C. L., and Unwin, P. R. (2019). Correlative electrochemical microscopy of Li-ion (de)intercalation at a series of individual $LiMn_2O_4$ particles. *Angew. Chem.* 131, 4654–4659. doi: 10.1002/ange.201814505

Totir, D. A., Bae, I. T., Hu, Y., Antonio, M. R., Stan, M. A., and Scherson, D. A. (1997). *In situ* Fe K-edge X-ray absorption fine structure of a pyrite electrode in a Li/polyethylene oxide($LiClO_4$)/FeS_2 battery environment. *J. Phys. Chem. B* 101, 9751–9756. doi: 10.1021/jp971470r

Tripathi, A. M., Su, W.-N., and Hwang, B.-J. (2018). *In situ* analytical techniques for battery interface analysis. *Chem. Soc. Rev.* 47, 736–851. doi: 10.1039/C7CS00180K

Tsai, P.-C., Wen, B., Wolfman, M., Choe, M.-J., Pan, M. S., Su, L., et al. (2018). Single-particle measurements of electrochemical kinetics in NMC and NCA cathodes for Li-ion batteries. *Energy Environ. Sci.* 11, 860–871. doi: 10.1039/C8EE00001H

Tu, Z., Choudhury, S., Zachman, M. J., Wei, S., Zhang, K., Kourkoutis, L. F., et al. (2018). Fast ion transport at solid–solid interfaces in hybrid battery anodes. *Nat. Energy* 3, 310–316. doi: 10.1038/s41560-018-0096-1

Vuillemin, B., and Bohnke, O. (1994). Kinetics study and modelling of the electrochromic phenomenon in amorphous tungsten trioxide thin films in acid and lithium electrolytes. *Solid State Ion.* 68, 257–267. doi: 10.1016/0167-2738(94)90184-8

Wang, H., Jang, Y.-I., Huang, B., Sadoway, D. R., and Chiang, Y.-M. (1999). TEM study of electrochemical cycling-induced damage and disorder in $LiCoO_2$ cathodes for rechargeable lithium batteries. *J. Electrochem. Soc.* 146:473. doi: 10.1149/1.1391631

Wang, J., Khoo, E., Lee, P. S., and Ma, J. (2008). Synthesis, assembly, and electrochromic properties of uniform crystalline WO_3 nanorods. *J. Phys. Chem. C* 112, 14306–14312. doi: 10.1021/jp804035r

Wen, R.-T., Granqvist, C. G., and Niklasson, G. A. (2015). Eliminating degradation and uncovering ion-trapping dynamics in electrochromic WO_3 thin films. *Nat. Mater.* 14, 996–1001. doi: 10.1038/nmat4368

Wolf, M., May, B. M., and Cabana, J. (2017). Visualization of electrochemical reactions in battery materials with X-ray microscopy and mapping. *Chem. Mater.* 29, 3347–3362. doi: 10.1021/acs.chemmater.6b05114

Wood, K. N., Kazyak, E., Chadwick, A. F., Chen, K.-H., Zhang, J.-G., Thornton, K., et al. (2016). Dendrites and pits: untangling the complex behavior of lithium metal anodes through operando video microscopy. *ACS Cent. Sci.* 2, 790–801. doi: 10.1021/acscentsci.6b00260

Wu, Y., and Liu, N. (2018). Visualizing battery reactions and processes by using *in situ* and in operando microscopies. *Chem* 4, 438–465. doi: 10.1016/j.chempr.2017.12.022

Xie, Z.-H., Jiang, Z., and Zhang, X. (2017). Review—promises and challenges of *in situ* transmission electron microscopy electrochemical techniques in the studies of lithium ion batteries. *J. Electrochem. Soc.* 164, A2110–A2123. doi: 10.1149/2.1451709jes

Yau, A., Cha, W., Kanan, M. W., Stephenson, G. B., and Ulvestad, A. (2017). Bragg coherent diffractive imaging of single-grain defect dynamics in polycrystalline films. *Science* 356, 739–742. doi: 10.1126/science.aam6168

Yu, X., Wang, R., He, Y., Hu, Y., Li, H., and Huang, X. (2010). Electrochromic behavior of transparent Li[sub 4]Ti[sub 5]O[sub 12]/FTO electrode. *Electrochem. Solid State Lett.* 13:J99. doi: 10.1149/1.3430658

Yu, Y., Xin, H. L., Hovden, R., Wang, D., Rus, E. D., Mundy, J. A., et al. (2012). Three-dimensional tracking and visualization of hundreds of Pt–Co fuel cell nanocatalysts during electrochemical aging. *Nano Lett.* 12, 4417–4423. doi: 10.1021/nl203920s

Yu, Y.-S., Farmand, M., Kim, C., Liu, Y., Grey, C. P., Strobridge, F. C., et al. (2018). Three-dimensional localization of nanoscale battery reactions using soft X-ray tomography. *Nat. Commun.* 9:921. doi: 10.1038/s41467-018-03401-x

Yuan, Y., Amine, K., Lu, J., and Shahbazian-Yassar, R. (2017). Understanding materials challenges for rechargeable ion batteries with *in situ* transmission electron microscopy. *Nat. Commun.* 8:15806. doi: 10.1038/ncomms15806

Zaghib, K., Mauger, A., Goodenough, J. B., Gendron, F., and Julien, C. M. (2007). Electronic, optical, and magnetic properties of $LiFePO_4$: small magnetic polaron effects. *Chem. Mater.* 19, 3740–3747. doi: 10.1021/cm0710296

Zeng, Z., Barai, P., Lee, S.-Y., Yang, J., Zhang, X., Zheng, W., et al. (2020). Electrode roughness dependent electrodeposition of sodium at the nanoscale. *Nano Energy* 72:104721. doi: 10.1016/j.nanoen.2020.104721

Zeng, Z., Liang, W.-I., Liao, H.-G., Xin, H. L., Chu, Y.-H., and Zheng, H. (2014). Visualization of electrode–electrolyte interfaces in $LiPF_6$/EC/DEC electrolyte for lithium ion batteries via *in situ* TEM. *Nano Lett.* 14, 1745–1750. doi: 10.1021/nl403922u

Zhang, R., Liu, B., Yang, A., Zhu, Y., Liu, C., Zhou, G., et al. (2018). *In situ* investigation on the nanoscale capture and evolution of aerosols on nanofibers. *Nano Lett.* 18, 1130–1138. doi: 10.1021/acs.nanolett.7b04673

Zhang, W., Seo, D.-H., Chen, T., Wu, L., Topsakal, M., Zhu, Y., et al. (2020). Kinetic pathways of ionic transport in fast-charging lithium titanate. *Science* 367, 1030–1034. doi: 10.1126/science.aax3520

Conflict of Interest: The authors declare that the research was conducted in the absence of any commercial or financial relationships that could be construed as a potential conflict of interest.